RSC Advances

ROYAL SOCIETY OF CHEMISTRY

www.rsc.org/advances

Table of Contents Figure

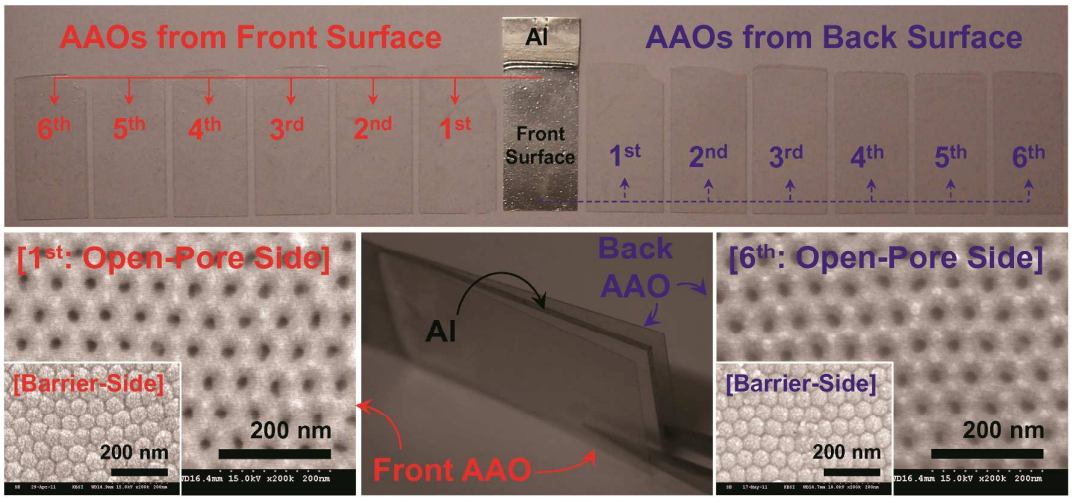

High-yield and environment-minded fabrication of nanoporous AAO templates through simultaneous multi-surface anodization and direct detachment by applying stair-like reverse biases.

RSC Advances

RSCPublishing

PAPER

High-Yield and environment-minded fabrication of nanoporous anodic aluminum oxide templates

Cite this: DOI: 10.1039/xoxxooooox

Young Ki Hong,[ab] Bo Hyun Kim,[a] Dong Il Kim,[a] Dong Hyun Park,[ac] and Jinsoo Joo*[a]

Received ooth January 2012,
Accepted ooth January 2012

DOI: 10.1039/xoxxooooox

www.rsc.org/

Nanoporous anodic aluminum oxide (AAO) templates, fabricated via anodization, have been widely studied in fundamental science and industry, for use as functional nanostructures in opto-electronics, membrane filters, energy storage devices, bio-applications, magnetic memory, etc. However, conventional AAO fabricating techniques have several disadvantages, such as the relatively long time required, inefficient usage of resources, and their toxicities, which restrict their practical application. This paper reports on a high-yield and environment-minded fabrication method for nanoporous AAO templates, accomplished through simultaneous multi-surface anodization and direct detaching of AAOs from an aluminum (Al) substrate by applying stair-like reverse biases in one electrolyte. These procedures can be repeated for mass production (*i.e.*, high yield) using the same Al substrate. The nanoporous AAO templates fabricated here were used to synthesize gold (Au) nanowires (NW) with a diameter of ~25 nm. This development, together with the modulation of physical properties of Au NWs, can enrich the potential of future nanotechnology based on nanoporous templates, and can also contribute to green technology owing to its minimized toxicity as well as its efficient use of resources.

Introduction

Anodization has been defined as the electric field-assisted local dissolution[1] and/or viscous flow[2] of anodic oxides under acidic electrolytes.[3] During this process, periodic nanopores with a high aspect ratio can be produced in the middle of hexagonal unit cells. These cells self-arrange in periodic honeycomb structures through repulsive interactions between adjacent unit cells, owing to volume expansion during oxidation as well as the displacement of anodic oxides driven by large compressive stresses due to a high electric field.[1-8] After the report on two-step anodization by Masuda and co-workers,[9,10] it became possible to extend the self-ordering regime owing to the texturing effect of pre-anodization.[3,4,11] Nanoporous anodic aluminum oxides (AAO) with self-assembled periodic honeycomb structures[1-7] have been intensively studied for their potential as universal templates for various functional nanostructures,[3,12-19] membrane filters,[20-23] energy storage devices,[24-27] bio-applications,[28-30] and magnetic memory.[31]

However, from the point of view of manufacturing nanoporous templates, conventional AAO fabricating techniques have several disadvantages, including the relatively long time required, the inefficient usage of resources, and their toxicities. The low yield and slow growth rates (2–10 μm h^{-1}) seen in AAO fabrication through conventional anodization (so-called mild anodization) were due to the relatively low anodic voltages corresponding to the types of acidic electrolytes used.[3,7,9,32] To improve the efficiency of these mild anodization techniques, higher anodic voltages and/or more highly concentrated acidic electrolytes (so-called hard anodization) were proposed. These methods showed distinct improvements in AAO growth rates (for example, 50–100 μm h^{-1} under oxalic acid[33,34] and 4–10 μm min^{-1} under phosphoric acid[35]) as well as improvements in the nanopore periodicities.[33-37] Heating problems due to the high applied current densities in the hard anodization techniques have required cooling apparatus[33,34] or additional cooling agents in the acidic electrolyte[35] in order to avoid the burn-out of the AAO.[38,39]

In both mild and hard anodization techniques, chemical etching for the separation of the AAO from the aluminum (Al) substrate has conventionally been performed using toxic reagents including heavy metal ions, such as mercury chloride ($HgCl_2$) or copper chloride ($CuCl_2$), resulting in longer process times and contaminated AAOs that can be hazardous.[1,5,6,9-11,18,22,25,32,34,35,37,40] Direct detachment of the AAO layer from the Al substrate by applying a pulse-type anodic bias have been reported.[41-45] However, butanedione and/or perchloric acid used as detaching electrolytes, which are also toxic and highly reactive. In addition, changing the electrolytes between the

anodization and detaching procedures is inefficient. Conventional anodization and separating/detaching techniques have produced a mono-surface AAO template from an Al substrate, which also restricts the efficiency of AAO fabrication as well as its applications.[1-11,18,22,25,31-47]

In this research, a high-yield and environment-minded fabrication process is demonstrated for nanoporous AAO templates, which were produced by simultaneous multi-surface anodization (SMSA) and direct detaching of AAOs from an Al substrate by applying stair-like reverse biases (SRB) in the same electrolyte used for anodization. These procedures can be repeated for mass production (*i.e.*, high yield) using the same Al substrate. The nanoporous AAO templates fabricated here were used to synthesize gold (Au) nanowires (NW) with a diameter of 25 nm. The surface plasmon (SP) absorption characteristics of the Au NWs with various diameters were also studied.

Experimental

Anodization and detachment of AAO

The anodization and detaching system consists of a double-jacket beaker (1 L), magnetic stirrer, programmable DC power supply (EDP-1500, PNSYS Co., Ltd.), and a low-temperature bath circulator (DTRC-640, JEIOTECH). Temperatures were controlled by the double-jacket beaker connected to a bath circulator using a solution of ethanol (95%) and deionized (DI) water (1 : 1, v/v) as the circulating media. Platinum (Pt) wire with a diameter of 1.0 mm and length of 50.0 mm was used as a counter electrode (Fig. 1a). The forward biases (Al: positive electrode, Pt: negative electrode) for electropolishing and anodization, and reverse biases (Al: negative electrode, Pt: positive electrode) for AAO detachment were applied using a programmable DC power supply controlled by an RS-232C interfaced PC program. Purified Al (Goodfellow, 99.99% purified) plates (width × length × thickness = 20.0 mm × 50.0 mm × 1.0 mm) were ultra-sonicated in acetone for 30 min and rinsed with DI water in order to eliminate organic residues on the surfaces. For minimizing the surface roughness, the multiple surfaces of a single Al plate were simultaneously electropolished by applying +20 V while in a solution of perchloric acid (60%) and absolute ethanol ($HClO_4$: C_2H_5OH = 1 : 4, v/v)[4,9,10] at 7 °C for less than 5 min. The electropolished multi-surfaces were pre-anodized by applying +25.0 V in a sulfuric acid aqueous solution (0.3 M) at 0 °C with vigorous magnetic stirring (800–1000 rpm).[7,32,36,40] To monitor the current-time (*I*–*t*) characteristic behavior of the SMSA, the pre-anodization times were fixed at 15 h. For mass production of AAOs, the pre-anodization times were reduced to 7 h 30 min. The nanoporous AAO layers produced by the pre-SMSA were chemically etched in a chromic acid aqueous solution (H_3PO_4 : CrO_3 = 0.56 M : 0.18 M) at 60 °C for ~3 h. Then, the main-SMSA was performed for 15 h under the same conditions as the pre-SMSA (+25 V, 0.3 M at 0 °C). The numbers of surfaces for anodization on the same Al plate were controlled by coating nail polish on designated surfaces and their corresponding edges.[10]

For the detachment of AAOs from the five surfaces of a single Al plate, SRBs were applied to the Al plate in the same sulfuric acid electrolyte used for anodization. The SRB applied times were selected by considering the *I*–*t* characteristic behaviors during the detaching procedure (for example, 10 min at –15.0 V, 7 min 30 s at –16.0 V, and 1 min 50 s at –17.0 V, as shown in Fig. 2a). After the detachment of the AAO layers, the residual alumina on the Al plate was eliminated in a chromic acid aqueous solution at 60 °C for 30 min. The remaining Al plate was re-used for the next AAOs fabrication. The electrolyte can be used for one whole sequence, which was defined in Fig. 3, and changed to a fresh one (optional).

Fabrication of Au NWs with various diameters

For selective removal of the barrier oxides at the bottom of the nanopores without causing nanopore-widening effects, the barrier side of the AAO was floated on a 2.0 M sodium hydroxide solution for a few seconds. Then, a thin Au layer was thermally evaporated on one side of the AAO template under high vacuum conditions (≤ 2.0×10^{-5} torr). Using these AAO templates, Au NWs with a diameter of ~25 nm were synthesized through an electrochemical deposition method using cyclic voltammetry (EC Epsilon, Bioanalytical Systems Inc.).[16,48] For comparison, AAO template with a nanopore diameter of ~250 nm were per-

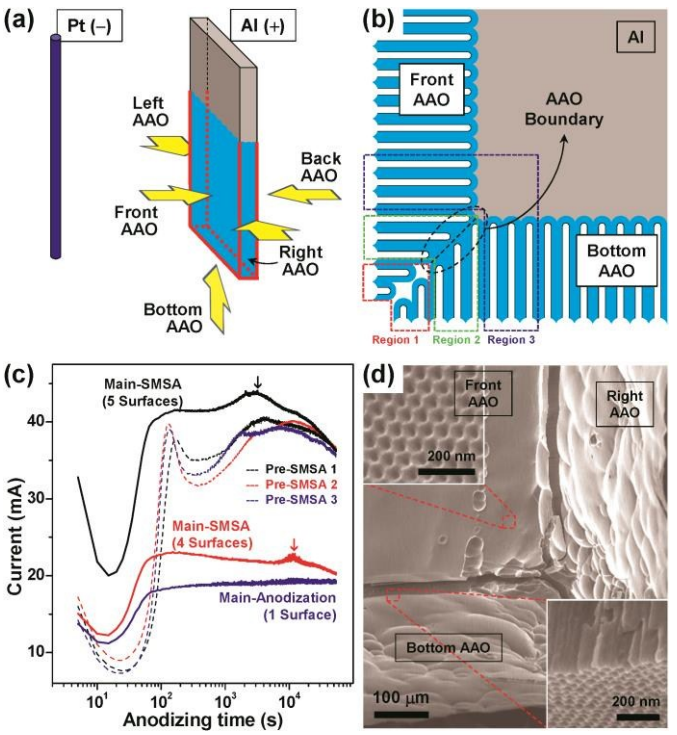

Fig. 1 (a) Schematic configuration of SMSA using a single Al plate as a working electrode (+) and a Pt wire as a counter electrode (–). The growth directions of the nanopores are represented as yellow arrows. (b) Schematic cross-sectional view of the adjacent front and bottom sides of the AAOs in the main-anodized Al plate. (c) *I*–*t* characteristic curves of the pre- and main-anodization procedures on various multiple surfaces. The arrows represent the current peaks due to boundary formation. (d) A corner view of the SEM image after the main-SMSA of the Al plate formed with nanoporous AAOs. Top inset: Magnified SEM image of the open-pore side of the nanoporous AAO from the front surface. Bottom inset: Magnified SEM images of the cracked edge between the front and bottom AAOs.

chased from Whatman Co. The current density was set to ~2.0 mA cm^{-2} and the applied voltage was ~1.20 (±0.05) V with respect to the Ag/AgCl reference electrode. The electrolyte for the synthesis of Au NWs was made using an Orotemp 24 gold plating solution purchased from Technic Inc. To obtain isolated strands of Au NWs, AAO templates were removed using a 2.0 M hydrofluoric acid solution.

Characterization

The *I*–*t* characteristic curves for the anodization and detachment procedures were recorded using a programmable DC power supply with RS-232C interfaced PC program. The formation of the nanopores of the AAOs, the morphological variations of the Al surfaces during the anodization and detachment procedures, and the formation of Au NWs were investigated using scanning electron microscope (SEM; JSM-5200, JEOL) images. The SP absorption properties of the Au NWs dispersed in methanol were investigated through ultraviolet-visible (UV-Vis) absorption spectra (HP 8453).

Results and discussion

Simultaneous multi-surface anodization

An electric field in the SMSA procedure was applied in the normal direction of each Al surface, and nanopores were formed in the same directions on multiple surfaces simultaneously, as shown in Fig. 1a and b. At the beginning of SMSA, barrier oxide layers on one surface (*e.g.*, the front surface) met and pushed away those in other surfaces (*e.g.*, the bottom and side surfaces) and vice versa, owing to the growth and volume expansion of the AAOs (regions 1 and 2 in Fig. 1b).[2-7,36] The boundaries between the AAO layers were formed along the edges of the Al plate (region 2 in Fig. 1b). As SMSA proceeded, the barrier oxide layers of the inner nanopores on perpendicular surfaces met continuously and the AAO boundaries on the edges of the Al substrate were diagonally extended inside the Al plate (region 3 in Fig. 1b). Previously formed boundaries continuously changed to cracks (region 1 in Fig. 1b) and mechanical stresses were applied to the multi-interfaces between the corresponding AAOs and Al surfaces, due to the volume expansions of the AAOs.

Fig. 1c compares the *I*–*t* characteristic curves for SMSA and conventional mono-surface anodization. In the pre-SMSA stage, using three different Al plates, the current peaks observed at the early stage (100–200 s) are typical features due to texturing effects resulting from the decrease of initial pore density with the steady-state nanopore growth (dotted curves in Fig. 1c).[3,4] The broad current peaks at the next stage (10^3–10^4 s), while still in the pre-SMSA stage, are due to the interactions between barrier oxides during simultaneous boundary formation. In the main-SMSA stage on the five surfaces, the current peak was clearly observed at ~3.0×10^3 s (black solid curve in Fig. 1c). In the main-SMSA stage on the four surfaces (*e.g.*, the back surface including its corresponding edges was coated with nail polish to protect against main-anodization), the current level (red solid curve in Fig. 1c) decreased as a result of the reduction of the anodizing surface area and the current peak was shifted to a later time (1.15×10^4 s). The current peak while anodizing five surfaces was observed at an earlier time, because the stresses were applied to more edges and/or more boundaries. The amount of stress during anodic oxidation is proportional to the anodizing area/time, and the current peak seen at a later time would be correlated with the equilibrium of stresses from adjacent surfaces. As shown in Fig. 1a, the area of the side surface (50.0 mm × 1.0 mm) is much smaller than that of the front (or back) surface (20.0 mm × 50.0 mm). To approach the equilibrium state in SMSA on four surfaces, it might take more time for the side surface to have sufficient stress (*i.e.*, more oxidation), thus pushing back the front surface owing to the absence of stress-support from the back surface. The gradual decrease of the current levels after longer times for both the pre- and main-SMSA results from the decrease of the total anodizing area. In addition, the suppression of ion migration due to the stresses stored in the SMSA also influences on the *I*–*t* characteristics (see also ESI and Fig. S1). The current peak was not observed in the main-anodization for only the front surface because there were no edges, and the *I*–*t* characteristic curve shows a typical saturated behavior (blue solid curve in Fig. 1c).[3,4]

Fig. 1d shows a corner view of an SEM image for the AAO surfaces (front, bottom, and right sides) after the first main-anodization on five surfaces. The formation of periodic nanopores with diameters of ~24 nm was observed on the front surface (top inset of Fig. 1d). The cracked edges between adjacent surfaces are clearly identified, as shown in Fig. 1d and its bottom inset.

Direct detachment of AAO from Al by Stair-like reverse biases

Fig. 2a shows the *I*–*t* characteristic curves during the detachment of AAOs from the Al plate by applying SRBs in a sulfuric acid

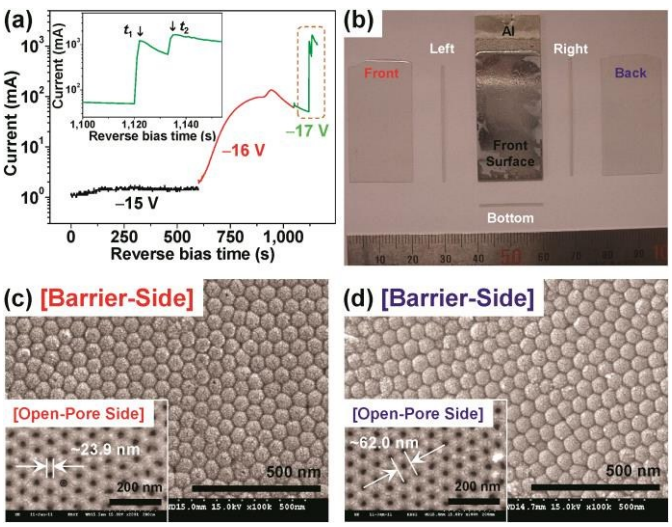

Fig. 2 (a) *I*–*t* characteristic curve during the detachment of AAOs from the Al plate by applying SRBs. Inset: Magnification of the *I*–*t* curve at −17.0 V. The arrows indicate the detachment time of the front (t_1 = 1,230 s) and back (t_2 = 1,650 s) AAO surfaces. (b) A photograph of five detached AAOs and the Al plate. (c, d) Barrier-side SEM images of the AAOs obtained from the (c) front and (d) back surface. Insets: Open-pore-side SEM images of the corresponding AAOs.

electrolyte. The relatively low current level (≤ 1.5 mA) at the beginning reverse bias (−15.0 V) was due to the cracks between AAO layers not reaching the Al edges and the dissolution of AAO boundaries not being fully activated. With reverse biases above a certain threshold (for example, −16.0 V in this case), the current level dramatically increased to a peak point and bubbling was observed at the edges because of boundary dissolution. After the peak point, the *I*–*t* curve decreased even for increasing reverse biases up to −17.0 V. The abrupt steps in the current level (at t_1 = 1,230 s and t_2 = 1,650 s) indicate the detachment of the AAO layers from the front and back surfaces, respectively. The electric fields of the SRBs might be more efficiently applied to the edges and vertexes of the samples, rather than the concaves on the Al surfaces. After the AAO boundaries were dissolved out, the permeation of electrolyte and the bubbling effects were extended to the inner areas along the multi-interfaces between the AAOs and Al surfaces, resulting in the detachment of AAOs. The stresses stored on the multi-interfaces were released owing to the removal of the AAO boundaries, which also assisted the detaching process. It should be noted that the typical features of the *I*–*t* characteristics curves were reproducible for all detaching procedures (see ESI Fig. S2). The SRBs could optimally accelerate the dissolution of oxide boundaries, resulting in the successful detachment of each AAO as a single piece with equal width and length of anodized area. It is noted that the AAO detachment was not reproducible with applying constant reverse bias. Fig. 2b shows a photograph of five detached AAO pieces with equal sizes for corresponding surfaces and the remaining Al plate. Periodic hexagonal arrangements of the barrier-oxides were observed for the as-detached AAOs from the front and back surfaces (Fig. 2c and d), indicating that the cleavage planes were beneath the barrier oxides. These results are different from previous reports, in which the detachment by pulse-type anodic bias in perchloric acid-based electrolytes occurred in the plane above the barrier oxides.[41-45] The diameter of the nanopores (D_p) and the interpore distance (D_{int}) of the AAOs fabricated here were ~23.9 nm and ~62.0 nm, respectively (insets of Fig. 2c and d). The thickness of the AAOs was ~80 μm and the growth rate was ~5.3 μm h^{-1}, indicating a mild anodization regime.

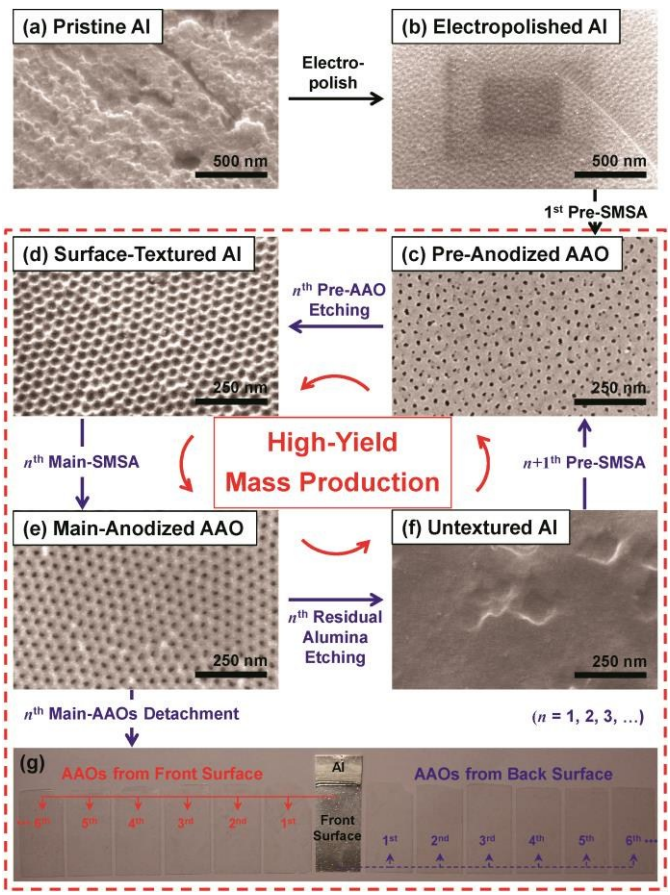

Fig. 3 The entire AAO fabrication procedure. (a–f) Surface morphology variation at each stage of the AAO fabrication procedure. SEM images of the front surface for the (a) pristine Al substrate, (b) electropolished Al substrate, (c) pre-anodized AAO (open-pore side), (d) textured Al substrate after removal of pre-AAO, (e) main-anodized AAO (open-pore side), and (f) untextured Al substrate after detachment of main-AAO and removal of residual alumina. (g) Photographs of twelve AAO templates obtained from the front and back surfaces after six repetitions of the sequence.

Morphological variation of multi-surfaces in SMSA

Fig. 3 presents the morphological variation of the Al surface corresponding to each stage of the AAO fabrication procedure. The mechanically polished pristine Al substrate displayed a rough surface, as shown in Fig. 3a. After electropolishing, the surface roughness markedly decreased and very small concaves with irregular shape and distribution, *i.e.*, a scallop pattern, were observed in Fig. 3b.[46] Fig. 3c shows an SEM image of the open-pore side view of the pre-anodized AAO on the Al front surface. The growth of nanopores in the pre-anodization stage was initiated in the concaves of the scallop pattern. As pre-anodization proceeded, nanopores were continually merged with adjacent nanopores, resulting in the decrease of initial nanopore density and increase of nanopore diameter. The size, shape, and distribution of nanopores in the upper parts were different with those in the lower parts in the same batch.[3,4] However, after removal of the pre-AAO layer by chemical etching, the Al surface was wholly textured with hexagonal concaves with relatively long-range periodicity (Fig. 3d). As shown in Fig. 3e, nanopore diameters and interpore distances of the main-anodized AAO were in good agreement with the results in Fig. 1 and 2. The textured features on the Al surface were destroyed by the SRB detaching procedure (Fig. 3f), which can be attributed to the fact that the concentration of Al^{3+} ions in the acidic electrolyte increased during two-step anodization[1,3,4] and that the reverse biases led to reduction of Al on surface. The texturing of the surface was successfully recovered by the next pre-anodization procedure (see ESI Fig. S7). It should be noted that all the SEM images in Fig. 3 were taken at the front surface. However, the above discussion about morphological variation was also confirmed from other surfaces through the SMSA procedure (see Fig. S3-S7 in ESI for more details).

Mass production of AAOs using SMSA and SRB

Fig. 3 also presents a flow chart of the entire procedure of AAO fabrication. The electropolishing and first pre-SMSA can be

categorized as a preliminary treatment. The individual sequence for fabricating one set of AAOs from multiple surfaces consists of (i) n^{th} chemical etching of pre-AAOs, (ii) n^{th} main-SMSA, (iii) n^{th} main-AAOs detachment by applying SRBs, (iv) n^{th} chemical etching of residual alumina, and (v) n+1th pre-SMSA (red dashed box in Fig. 3), where n denotes the number of the applied sequence (n = 1, 2, 3…). For higher yield and mass production of AAOs, the above sequence was repeated six times using the same single Al plate in the sulfuric acid electrolyte. In total, twelve AAOs were successfully obtained from the front and back surfaces, excluding AAOs from the side and bottom surfaces, as shown in Fig. 3g. These demonstrated the capacity for mass production using this method. The thickness of the remaining Al plate was ~200 μm, suggesting further productions of AAO templates.

Fig. 4 shows SEM images of the nanoporous AAOs obtained from the front and back surfaces through the first to sixth sequences using the same Al plate. The average D_p and D_{int} of these AAOs were almost the same for all sequences at approximately 23.9 nm and 62.0 nm, respectively. The nanopore density $\left(\rho_p = \{2/\sqrt{3}\, D_{int}^2\} \times 10^{14}\ \mathrm{cm}^{-2}\right)$ and porosity $\left(P\ (\%) = (\pi/2\sqrt{3})(D_p/D_{int})^2\right)$ were estimated to be 3.0×10^{14} cm^{-2} and 13.4%, respectively, which agree well with previous reports on mono-surface anodization.[3,7,33,47]

Surface plasmon properties of Au NWs with various diameters

Using the fabricated AAOs as nanoporous templates, Au NWs were synthesized using the electrochemical deposition method.[16,48] Fig. 5a shows an SEM image of the Au NWs with a diameter (ϕ) of ~25 nm, which is the same diameter of the nano-

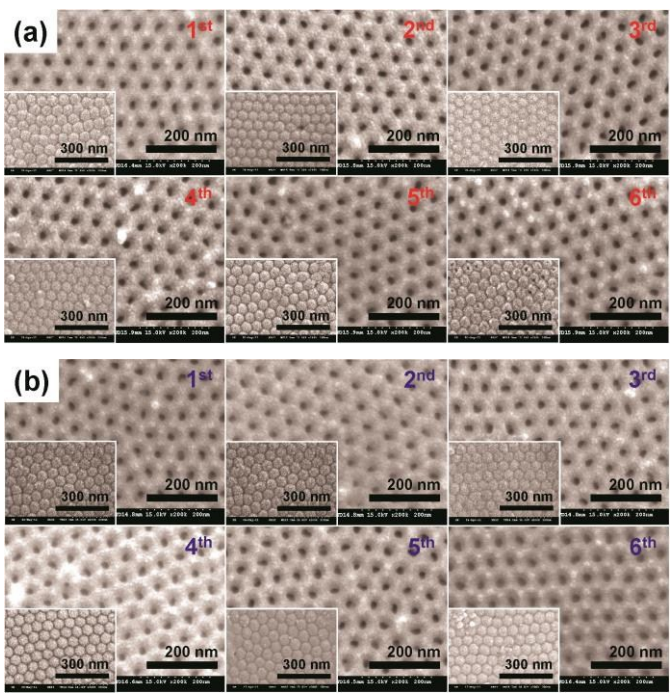

Fig. 4 SEM images of the open-pore sides on the (a) front and (b) back nanoporous AAO surfaces obtained from the first through to the sixth SMSA using the same Al plate. Insets: SEM images of the barrier sides on the corresponding samples.

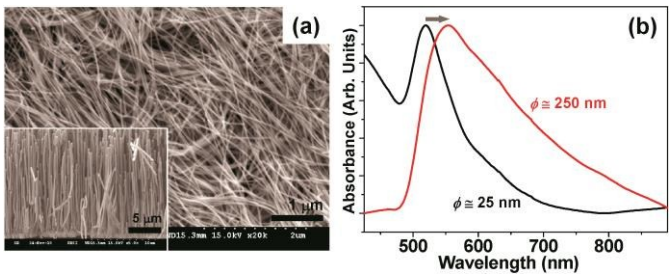

Fig. 5 (a) SEM image of Au NWs synthesized using the fabricated nanoporous AAO template ($\phi \cong 25$ nm). Inset: SEM image of Au NWs synthesized using the purchased AAO templates ($\phi \cong 250$ nm). (b) Normalized UV-Vis absorption spectra of Au NWs with different diameters.

pores in the AAO templates. For comparison, Au NWs with a diameter of ~250 nm were synthesized through the same method using purchased AAO templates (Whatman Co.; $\phi \cong 250$ nm) (inset of Fig. 5a). Looking at the UV-Vis absorption spectra in Fig. 5b, the main peak, originated from the transverse modes of SP absorption, was observed at ~520 nm for the thin Au NWs ($\phi \cong 25$ nm). The peak shifted to ~553 nm for the thick Au NWs ($\phi \cong 250$ nm). As the diameter of the Au NWs increased, the main SP absorption peaks became broadened, implying that the longitudinal modes of SP absorption for longer wavelengths were enhanced, depending on the diameters of the NWs.[16,49,50]

Conclusions

In summary, this research demonstrated a new method for fabricating nanoporous AAO templates. This method included the sequential repetition of SMSA followed by SRBs on multiple surfaces of a single Al plate, without changing the electrolyte. The advantages of this work in fabricating AAOs include the potential for mass production, minimized toxicity, and simplicity, as well as the efficient usage of resources. The SMSA combined with SRB method also exhibited excellent performance under oxalic acid conditions. The yield of the fabrication of AAOs based on this method can be enhanced by using a regular hexahedral Al and hard anodization conditions after solving any heating problems. The nanoporous AAO templates fabricated here exhibited a regular diameter and length of nanopores, making them useful as universal templates with diverse applications.

Acknowledgements

This study was supported by Global Frontier Program through the National Research Foundation of Korea (NRF) funded by the Ministry of Science, ICT & Future Planning (2014M3A6B3063710).

Notes and references

[a]Department of Physics, Korea University, Seoul 136-713, South Korea.
[b]Department of Electronics and Radio Engineering, Kyung Hee University, Gyeonggi 446-701, South Korea.
[c]Department of Applied Organic Materials Engineering, Inha University, Incheon 402-751, South Korea.

Electronic Supplementary Information (ESI) available: Detailed investigations of the reproducibility of *I–t* characteristic behaviors in SMSA and SRB-based detachment from the first to the sixth sequences and morphological variation at each stage of the AAO fabricating procedure are reported. See DOI: 10.1039/b000000x/

1 J. P. O'Sullivan and G. C. Wood, *Proc. R. Soc. London A*, 1970, **317**, 511-543.
2 J. E. Houser and K. R. Hebert, *Nature Mater.*, 2009, **8**, 415-420.
3 W. Lee and S.-J. Park, *Chem. Rev.*, 2014, **114**, 7487-7556.
4 F. Li, L. Zhang and R. M. Metzger, *Chem. Mater.*, 1998, **10**, 2470-2480.
5 O. Jessensky, F. Müller and U. Gösele, *Appl. Phys. Lett.*, 1998, **72**, 1173-1175.
6 A. P. Li, F. Müller, A. Bimer, K. Nielsch and U. Gösele, *J. Appl. Phys.*, 1998, **84**, 6023-6026.
7 K. Nielsch, J. Choi, K. Schwirn, R. B. Wehrspohn and U. Gösele, *Nano Lett.*, 2002, **2**, 677-680.
8 K. R. Hebert, S. P. Albu, I. Paramasivam and P. Schmuki, *Nature Mater.*, 2012, **11**, 162-166.
9 H. Masuda and K. Fukuda, *Science*, 1995, **268**, 1466-1468.
10 H. Masuda and M. Satoh, *Jpn. J. Appl. Phys.*, 1996, **35**, L126-L129.
11 H. Asoh, K. Nishio, M. Nakao, T. Tamamura and H. Masuda, *J. Electrochem. Soc.*, 2001, **148**, B152-B156.
12 C. R. Martin, *Science*, 1994, **266**, 1961-1966.
13 S. G. Cloutier, P. A. Kossyrev and J. Xu, *Nature Mater.*, 2005, **4**, 887-891.
14 D. H. Park, M. S. Kim and J. Joo, *Chem. Soc. Rev.*, 2010, **39**, 2439-2452.
15 D. H. Park, Y. K. Hong, E. H. Cho, M. S. Kim, D. C. Kim, J. Bang, J. Kim and J. Joo, *ACS Nano*, 2010, **4**, 5155-5162.
16 M. R. Jones, K. D. Osberg, R. J. MacFarlane, M. R. Langille and C. A. Mirkin, *Chem. Rev.*, 2011, **111**, 3736-3827.
17 Y. K. Hong, D. H. Park, S. G. Jo, M. H. Koo, D. C. Kim, J. Kim, J. S. Kim, S. Y. Jang and J. Joo, *Angew. Chem. Int. Ed.*, 2011, **50**, 3734-3738.
18 M. Raoufi and H. Schönherr, *RSC Adv.*, 2013, **3**, 13429-13436.
19 X. Qu, Y. Hou, C. Wang, F. Du and L. Cao, *RSC Adv.*, 2015, **5**, 5307-5311.
20 L. J. Cote, R. Cruz-Silva and J. Huang, *J. Am. Chem. Soc.*, 2009, **131**, 11027-11032.
21 J. H. Oh, H. W. Lee, S. Mannsfeld, R. M. Stoltenberg, E. Jung, Y. W. Jin, J. M. Kim, J. B. Yoo and Z. Bao, *Proc. Natl. Acad. Sci. U. S. A.*, 2009, **106**, 6065-6070.
22 M. E. Warkiani, A. A. S. Bhagat, B. L. Khoo, J. Han, C. T. Lim, H. Q. Gong and A. G. Fane, *ACS Nano*, 2013, **7**, 1882-1904.
23 L. Lv, Y. Fan, Q. Chen, Y. Zhao, Y. Hu, Z. Zhang, N. Chen and L. Qu, *Nanotechnology*, 2014, **25**, 235401.
24 G. Che, B. B. Lakshmi, E. R. Fisher and C. R. Martin, *Nature*, 1998, **393**, 346-349.
25 R. Liu, J. Duay and S. B. Lee, *ACS Nano*, 2011, **5**, 5608-5619.
26 G. Cheng, Z. H. Lin, Z. L. Du and Z. L. Wang, *ACS Nano*, 2014, **8**, 1932-1939.
27 B. Han, S. Zhang, R. Zhou, X. Wu, X. Wei, Y. Xing, S. Wang and T. Qi, *RSC Adv.*, 2014, **4**, 50752-50758.
28 S. B. Lee, D. T. Mitchell, L. Trofin, T. K. Nevanen, H. Söderlund and C. R. Martin, *Science*, 2002, **296**, 2198-2200.
29 F. Matsumoto, K. Nishio and H. Masuda, *Adv. Mater.*, 2004, **16**, 2105-2108.
30 R. Poplausks, U. Malinovskis, J. Andzane, J. Svirksts, A. Viksna, I. Muiznieks and D. Erts, *RSC Adv.*, 2014, **4**, 48480-48485.
31 K. Nielsch, F. Müller, A. P. Li and U. Gösele, *Adv. Mater.*, 2000, **12**, 582-586.
32 H. Masuda, F. Hasegwa and S. Ono, *J. Electrochem. Soc.*, 1997, **144**, L127-L130.
33 W. Lee, R. Ji, U. Gösele and K. Nielsch, *Nature Mater.*, 2006, **5**, 741-747.
34 W. Lee, K. Schwirn, M. Steinhart, E. Pippel, R. Scholz and U. Gösele, *Nature Nanotech.*, 2008, **3**, 234-239.
35 Y. Li, M. Zheng, L. Ma and W. Shen, *Nanotechnology*, 2006, **17**, 5101-5105.
36 S. Z. Chu, K. Wada, S. Inoue, M. Isogai and A. Yasumori, *Adv. Mater.*, 2005, **17**, 2115-2119.
37 K. Schwirn, W. Lee, R. Hillebrand, M. Steinhart, K. Nielsch and U. Gösele, *ACS Nano*, 2008, **2**, 302-310.
38 S. Ono, M. Saito, M. Ishiguro and H. Asoh, *J. Electrochem. Soc.*, 2004, **151**, B473-A478.
39 S. Ono, M. Saito and H. Asoh, *Electrochem. Solid-State Lett.*, 2004, **7**, B21-B24.
40 S. Z. Chu, K. Wada, S. Inoue, M. Isogai, Y. Katsuta and A. Yasumori, *J. Electrochem. Soc.*, 2006, **153**, B384-B391.
41 J. H. Yuan, F. Y. He, D. C. Sun and X. H. Xia, *Chem. Mater.*, 2004, **16**, 1841-1844.
42 J. H. Yuan, W. Chen, R. J. Hui, Y. L. Hu and X. H. Xia, *Electrochim. Acta*, 2006, **51**, 4589-4595.
43 S. Zhao, K. Chan, A. Yelon and T. Veres, *Nanotechnology*, 2007, **18**, 245304.
44 W. Chen, J. S. Wu, J. H. Yuan, X. H. Xia and X. H. Lin, *J. Electroanal. Chem.*, 2007, **600**, 257-264.
45 L. Gao, P. Wang, X. Wu, S. Yang and X. Song, *J. Electroceram.*, 2008, **21**, 791-794.
46 M. T. Wu, I. C. Leu and M. H. Hon, *J. Vac. Sci. Technol., B*, 2002, **20**, 776-782.
47 Y. Sui and J. M. Saniger, *Mater. Lett.*, 2001, **48**, 127-136.
48 J. Joo, S. J. Lee, D. H. Park, Y. S. Kim, Y. Lee, C. J. Lee and S. R. Lee, *Nanotechnology*, 2006, **17**, 3506-3511.
49 M. Hu, J. Chen, Z. Y. Li, L. Au, G. V. Hartland, X. Li, M. Marquez and Y. Xia, *Chem. Soc. Rev.*, 2006, **35**, 1084-1094.
50 K. M. Mayer and J. H. Hafner, *Chem. Rev.*, 2011, **111**, 3828-3857.

